FACTA UNIVERSITATIS
Series:**Mechanical Engineering** Vol. 20, Nº 2, 2022, pp. 363 - 380
https://doi.org/10.22190/FUME220131021L

Original scientific paper

MULTI-SCALE NUMERICAL APPROACH TO THE POLYMER FILLING PROCESS IN THE WELD LINE REGION

Xuejuan Li[1], Dan Wang[1], Tareq Saeed[2]

[1]School of Science, Xi'an University of Architecture and Technology, Xi'an, China
[2]Nonlinear Analysis and Applied Mathematics (NAAM) Research Group, Department of Mathematics, Faculty of Science, King Abdulaziz University, Jeddah, Saudi Arabia

Abstract. *In this paper, a multi-scale coupling mathematical model is suggested for simulating the polymer filling process in the weld line region on a micro scale. The model considers two aspects: one is the coupling model based on stresses in the whole cavity region; the other is the multi-scale coupling model of continuum mechanics (CM) and the molecular dynamics (MD) in a weldline region. A weak variational formulation is constructed for the finite element method (FEM), which is coupled with the Verlet algorithm based on the domain decomposition technique. Meanwhile, an overlap region is designed so that the FEM and the MD simulations are consistent with each other. The molecular backbone orientation of the whole cavity is illustrated and the position of the weld line is determined by the characteristics of the molecular backbone orientation. Finally, the properties of the polymer chain in the weld line region are studied conformationally and dynamically. The conformational changes and movement process elucidate that the polymer chains undertake stretching, entangling and orientating. Moreover, the effect of the number of chains and melt temperature on the spatial properties of chain conformation are investigated.*

Key words: *Multi-scale method, Weld line, VMS-FEM, MD, Domain decomposition*

1. INTRODUCTION

The injection molding is a common polymer processing technology. However, the weld line is a common macro defect in polymer processing [1], and it is very difficult to avoid the occurrence of weld line when the products have an insert or the multi-gate technology is used. From the formation of the weld line, the macromolecular chain parallel to each other and the melt properties are different when two or more melt fronts meet. These may cause loose microstructure and stress concentration in the fusion zone, and further affect the

Received: January 31, 2022 / Accepted April 24, 2022
Corresponding author: Xuejuan Li
School of Science, Xi'an University of Architecture and Technology, Xi'an, 710055, China
E-mail: lxj_zk@163.com

products' mechanical, optical and thermal properties [2]. In order to control this defect and optimize the actual processing, the formation mechanism in processing should be revealed from the molecular orientation, molecular stretching, molecular chain entanglement and so on. Therefore, it is great significance to study the weldline's mechanical properties based on the characteristics of microstructure to improve the quality of the products. For this purpose, much literature was appeared using experiments alone [3-11], for examples, Minh et al. studied the weld line strength by using various venting systems in injection molding process [3]. Li, et al. [4] and Wang, et al. [5] proved that the rapid heat cycle molding (RHCM) was an effective way to improvement of the mechanical properties of weld lines. Mosey, et al. [6] and Hashimoto, et al. [7] researched the weldline reduction of injection based on different processing parameters. Baradi, et al. [8] and Liao, et al. [9] found that the experimental X-ray tomography provides us with an effective tool to ensuring the mechanical and geometrical characters of the weldlines and predict the location of weld lines via molecular orientation distribution. Oh, et al. [10] and Kalus, et al. [11] showed that the digital image is another useful technique to find weldline defects and can illustrate strain profiles in the weld line region. All these researches are extremely useful to show detailed microstructural characterization of the weld line region experimentally, however only experimental methods are not enough to have a deep physical insight into the polymer filling process in a weld line region.

Although much experimental achievement had been obtained by various advanced experiments, there are still many problems to be solved because of the limitation of experimental conditions, and many hidden mechanisms cannot be revealed by experiment alone, for examples, the chains' entangling, orientating and stretching.

Recent decades had seen the fast progress in computer simulation methods, and now the numerical simulation has become a powerful method to improve the quality and processing of polymer products [12-21]. Wang et al. [12] adopted FEM and the arbitrary Lagrangian-Eulerian (ALE) method to track the free surface of a polymer melt flow in the filling processing. Nguyen, et al. [13] and Yang, et al. [14] used numerical approaches to study the fiber orientation of the filling processing, and the finite volume method (FVM) was adopted to deal with the polymer melt process. Li, et al. [15] and Cao, et al. [16] used FEM/FVM and FEM to solve the flow-induced stress, respectively. Deng, et al. [17] pointed out that the Lattice Boltzmann method (LBM) can predict the injection molding process accurately. Farahani, et al. [18] applied the smoothed particle hydrodynamics (SPH) technology to study numerically the hybrid process of sheet metal forming and injection molding. Zhang, et al. [19] adopted the boundary element method (BEM) to complete the steady-state cooling simulation. Pashmforoush used Finite Element Analysis to study Carbon Fibers/Carbon Nanotubes Reinforced Polymer Composite [20]. Moreover, Li et al. [21] used a weak variational formulation based multi-scale finite element method (VMS-FEM) to predict successfully the polymer melt filling process. These numerical methods have their respective advantages in the application in the injection molding, and can make up for the defects of the experiment.

Above all, we know that there are many research findings for mechanical properties of a weldline region based on some experimental methods and various numerical methods in the injection molding. However, there is few studies on the numerical simulation of weld line region based on multi-scale modeling and calculation. The numerical simulation using multiple scales can reveal some hidden mechanisms which cannot be found using a single

macro scale, for example, a chain's stretching cannot be simulated by any a numerical method, and a molecule's scale must be used, which makes the numerical simulation impossible.

In our previous work [22], the double-equation eXtended Pom-Pom (DXPP) stress equation was adopted to describe the molecular orientation in the flow of polymer melt. It is known that some researches based on the molecule's scale are widely used in various areas [23-27]. Cocker et al. [24] tracked a single molecule's trajectory on a molecule's scale by femtosecond orbital imaging. Zhang, et al. [25] reported the isotropical expansion ability of macromolecular ferritin crystals with integrated hydrogel polymers. Moreover, the molecular dynamics (MD) simulation can reveal microstructure of the materials [28-30]. For example, Valiullin et al. [28] considered a transient sorption in a mesoporous material by the molecular dynamical technology. Zhao et al. applied the all atom molecular dynamics to simulate the HIV-1 capsid structure [29]. Zepeda-Ruiz, et al. studied metal plasticity by the fully dynamic atomistic simulation, and gave the limits conditions of dislocation-mediated plasticity [30]. However, it is not suitable for the problem of long calculation time due to huge computational cost.

Based on the above analysis, the numerical simulation of mechanical properties of weld line region based on multi-scale modeling and calculation will be studied in this paper. Meanwhile, the coupling model of the DXPP stress equation and governing equations of melt flow based on the stress is used to describe the molecular orientation in the whole mold cavity and help to distinguish the weld line region according to the characterization of molecules' orientation. Moreover, the polymer filling process is a two-phase flow problem have discontinuity of unknowns on the interfaces generated by the different material properties of the fluids. Multi-scale method with a pressure-enriched finite element shape function enables to simulate the different behavior of two fluids. So, the VMS-FEM is used to solve this coupling model. The MD method is adopted in the weld line region to obtain numerically the real molecules' information. Moreover, the coupling molding of continuum mechanics (CM) and MD is established based on the domain decomposition technology.

2. Multi-Scale Model for Polymer Filling Process

For the multi-scale model, the multiple scale concept means two aspects: one is the coupling model based on stresses in the whole cavity region excluding weld line, the other is the multi-scale coupling model of continuum mechanics and the molecular dynamics in the weld line region. Details are as below in this section.

2.1. The coupling model of the CM and DXPP model based on stresses

The polymer melt filling process follows laws in the continuum mechanics, i.e., the mass conservation law and the moment conservation law [22].The moment equation and the mass equation are

$$\begin{aligned}\frac{\partial(\rho\mathbf{u})}{\partial t}+\nabla\cdot(\rho\mathbf{uu})-\frac{1}{\mathrm{Re}}\nabla\cdot(\eta(\nabla\mathbf{u}+\nabla\mathbf{u}^{\mathrm{T}}))\\ =-\nabla\cdot p+H_{\varepsilon}(\varphi)\frac{1}{\mathrm{Re}}\nabla\cdot((1-\beta)\eta(\nabla\mathbf{u}+\nabla\mathbf{u}^{\mathrm{T}})+\nabla\cdot\boldsymbol{\tau})\end{aligned} \tag{1}$$

$$\nabla \cdot \mathbf{u} = 0 \tag{2}$$

where **u**, p, **τ**, Re, ρ, η, β and φ are, respectively, speed, pressure, and stress, Reynolds number, the density, viscosity, viscosity ratio and level set function. $H_\varepsilon(\varphi)$ [31] is given as

$$H_\varepsilon(\varphi) = \begin{cases} 0, & \varphi < -\varepsilon \\ \dfrac{1}{2}\left[1 + \dfrac{\varphi}{\varepsilon} + \sin(\pi\varphi/\varepsilon)/\pi\right], & \varphi \le \varepsilon \\ 1, & \varphi > \varepsilon \end{cases} \tag{3}$$

The average material parameters in gas-melt mixed zone can be written as

$$\begin{aligned} \rho(\varphi) &= \rho_g + (\rho_m - \rho_g)H_\varepsilon(\varphi) \\ \eta(\varphi) &= \eta_g + (\eta_m - \eta_g)H_\varepsilon(\varphi) \end{aligned} \tag{4}$$

The subscripts represent gas (g) and melt (m), respectively.

In order to obtain the molecular information in the whole filling cavity, we use the DXPP stress model to describe the molecular orientation (**S**) and stretch (**Λ**). In our previous research [22], we had simulated the DXPP model based on a benchmark problem. The DXPP equations read

$$\begin{aligned} &\mathrm{We}\left(\frac{\partial \mathbf{S}}{\partial t} + \mathbf{u}\cdot\nabla\mathbf{S} - \mathbf{S}\cdot\nabla\mathbf{u} - (\nabla\mathbf{u})^T\cdot\mathbf{S} + 2[\mathbf{D}:\mathbf{S}]\mathbf{S}\right) \\ &+ \frac{1}{\mathbf{\Lambda}^2}\left[3\alpha\mathbf{\Lambda}^4\mathbf{S}\cdot\mathbf{S} + (1-\alpha-3\alpha\mathbf{\Lambda}^4\mathrm{tr}(\mathbf{S}\cdot\mathbf{S}))\mathbf{S} - \frac{1-\alpha}{3}\mathbf{I}\right] = 0 \end{aligned} \tag{5}$$

$$\mathrm{We}\left(\frac{\partial \mathbf{\Lambda}}{\partial t} + \mathbf{u}\cdot\nabla\mathbf{\Lambda}\right) = \mathrm{We}\mathbf{\Lambda}(\mathbf{D}:\mathbf{S}) - re^{\nu(\mathbf{\Lambda}-1)}(\mathbf{\Lambda}-1) \tag{6}$$

where We is the Weissenberg number; **I** denotes the unit tensor; **D** is the deformation rate tensor; r is the relaxation time ratio; α is a material parameter, defining the amount of anisotropy; $\nu = 2/q$, where q is the amount of arms at the end of a backbone.

Eqs. (5) and (6) are the molecular orientation and stretch equation, respectively. The stresses tensor can be written as [22]

$$\boldsymbol{\tau} = \frac{1-\beta}{\mathrm{We}}(3\mathbf{\Lambda}^2\mathbf{S} - \mathbf{I}) \tag{7}$$

So, Eqs. (1), (2), (5)-(7) constitute the multi-scale coupled model based on stresses tensor. Our model can not only reveal the macro physics quantities, e.g., the velocity and the pressure, but also illustrate the micro molecular orientation and stretch.

2.2. The coupling model of the CM model and the MD model

The couple of CM and MD simulations is constructed for numerical study of the microstructural characterization of the weld line region in the polymer filling process, the latter is to solve atoms' motion [32]

$$m_i \frac{d^2 r_i}{dt^2} = F_i \quad i = 1, 2, \cdots, N \tag{8}$$

$$F_i = -\nabla E(r_1, r_2, \cdots, r_N) \tag{9}$$

where m_i, r_i, F_i and E are an atom's mass, displacement, force and the total potential energy, respectively. E consists of following components [32]

$$E = E_{\text{nb}} + E_{\text{bond}} + E_{\text{angle}} + E_{\text{torsion}} \tag{10}$$

$$\begin{cases} E_{\text{nb}} = \sum_{i<j} [q_i q_j e^2 / r_{ij} + 4\varepsilon_{ij}(d_{ij}^{12} / r_{ij}^{12} - d_{ij}^{6} / r_{ij}^{6})] f_{ij} \\ E_{\text{bond}} = \sum_{\text{bonds}} K_r (r - r_{\text{eq}})^2 \\ E_{\text{angle}} = \sum_{\text{angles}} K_\theta (\theta - \theta_{\text{eq}})^2 \\ E_{\text{torsion}} = \sum_i \frac{V_1^i}{2}[1 + \cos(\phi_i)] + \frac{V_2^i}{2}[1 - \cos(2\phi_i)] + \frac{V_3^i}{2}[1 + \cos(3\phi_i)] \end{cases} \tag{11}$$

where the subscripts i, j represent the atoms i and j , the subscript "eq" is the equilibrium point; q_i represents an atom's fixed charge, and r_{ij} is the distance between two atoms; The parameters d_{ij} and ε_{ij} are, respectively, the zero-energy distance and the minimal interaction energy; r and K_r are, respectively, its length and stiffness; θ and K_θ represent, respectively, the bond angel and the angle stiffness; V_n^i (n=1, 2, 3) are fitting parameters, and φ_i the improper dihedral angle.

For the domain decomposition technology, the whole calculation region is decomposed into 2 domains, one for the CM simulation, and the other for the MD simulation in Fig. 1. From this figure we can know that the shading domain represented by the skew lines is the domain of CM simulation region and the domain represented by the dots is the domain of MD. C→P is the left boundary of MD region, while P→C is the right boundary of CM region. The domain between of these two boundaries is the overlap region, and we assume that in this overlap region the description of two scales is consistent with the description of MD.

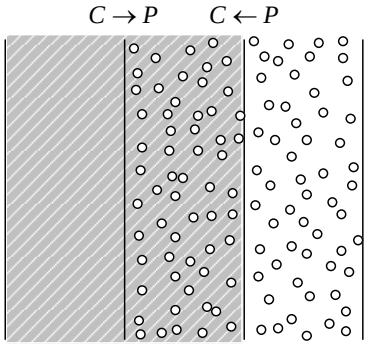

Fig. 1 The domain decomposition between the CM and MD simulations

The continuum assumption requires [33]

$$\frac{1}{N_J}\sum_i \mathbf{v}_i(t) = \mathbf{u}_J(t) \tag{12}$$

and

$$\frac{1}{N_J}\sum_i \ddot{\mathbf{x}}_i(t) = \frac{D\mathbf{u}_J(t)}{Dt} \tag{13}$$

where N_J is the number of molecules.

In order to satisfy this non-holonomic constraint, we modify Eq. (8) as follows

$$\ddot{\mathbf{x}}_i = \frac{\mathbf{F}_i}{m} - \frac{1}{N_J m}\sum_{i=1}^{N_J}\mathbf{F}_i + \frac{D\mathbf{u}_J(t)}{Dt} \tag{14}$$

and its discrete scheme is

$$\ddot{\mathbf{x}}_i = \frac{\mathbf{F}_i}{m} - \frac{1}{N_J}\sum_{i=1}^{N_J}\frac{\mathbf{F}_i}{m} - \frac{1}{\Delta t_{MD}}\left(\frac{1}{N_J}\sum_{i=1}^{N_J}\dot{\mathbf{x}}_i(t) - \mathbf{u}_J(t+\Delta t_{MD})\right) \tag{15}$$

where Δt_{MD} is the time step.

3. Numerical Method for Multi-Scale model

3.1. VMS - FEM in the ASGS stabilized formulation

For a general numerical method, the discontinuities of interfaces cannot be captured by standard interpolation functions. Moreover, the convective term of the momentum and the constitutive equations always lead to instabilities. Fortunately, a pressure-enriched finite element shape function enables to simulate the discontinuities of interfaces. The variational multi-scale method can stabilize the numerical approximation of the convective term. Therefore, a VMS-FEM method is used in this paper. The detailed derivation process is as follows.

We introduce U=[$\mathbf{u}$, p, $\mathbf{S}$, $\mathbf{\Lambda}$] and write Eqs. (1), (2), (5) and (6) in the form

$$\mathcal{D}_t(U) + \mathcal{L}(\mathbf{u}, \mathbf{S}, \mathbf{\Lambda}; U) = 0 \tag{16}$$

where

$$\mathcal{D}_t(U) := \begin{pmatrix} \rho\dfrac{\partial \mathbf{u}}{\partial t} \\ 0 \\ \mathrm{We}\dfrac{\partial \mathbf{S}}{\partial t} \\ \mathrm{We}\dfrac{\partial \mathbf{\Lambda}}{\partial t} \end{pmatrix}$$

and $\mathcal{L}(\hat{\mathbf{u}},\hat{\mathbf{S}},\hat{\Lambda};U) \coloneqq \begin{pmatrix} \rho\hat{\mathbf{u}}\cdot\nabla\mathbf{u} - \dfrac{2\eta}{\mathrm{Re}}(H_\varepsilon(\varphi)(\beta-1)+1)\nabla\cdot\mathbf{D} - \dfrac{H_\varepsilon(\varphi)}{\mathrm{Re}}\nabla\cdot\boldsymbol{\tau} + \nabla\cdot p \\ \nabla\cdot\mathbf{u} \\ \mathrm{We}(\hat{\mathbf{u}}\cdot\nabla\mathbf{S} - \mathbf{S}\cdot\nabla\hat{\mathbf{u}} - (\nabla\hat{\mathbf{u}})^T\cdot\mathbf{S}) + 2\mathrm{We}[\mathbf{D}\!:\!\mathbf{S}]\mathbf{S} \\ \qquad + \dfrac{1}{\boldsymbol{\Lambda}^2}\left[3\alpha\boldsymbol{\Lambda}^4\mathbf{S}\cdot\mathbf{S} + (1-\alpha-3\alpha\boldsymbol{\Lambda}^4\mathrm{tr}(\mathbf{S}\cdot\mathbf{S}))\mathbf{S} - \dfrac{1-\alpha}{3}\mathbf{I}\right] \\ \mathrm{We}\boldsymbol{\Lambda}(\mathbf{D}:\mathbf{S}) - \hat{\mathbf{u}}\cdot\nabla\boldsymbol{\Lambda} - re^{\nu(\boldsymbol{\Lambda}-1)}(\boldsymbol{\Lambda}-1) \end{pmatrix}$.

The system given in Eq. (16) is strongly nonlinear and it is difficult to establish a variational principle. In this paper, a weak variational theory is considered for Eq. (16), that is to find $U=[\mathbf{u}, p, \mathbf{S}, \boldsymbol{\Lambda}]\in X$ for all $V=[v, q, B, \chi]\in X$. The weak variational formulation of the problem can be written as

$$(\mathcal{D}_t(U),\mathbf{V}) + B(\mathbf{u},\mathbf{S},\Lambda;U,V) = 0 \tag{17}$$

for all $V\in X$, where:

$$\begin{aligned} B(\hat{\mathbf{u}},\hat{\mathbf{S}},\hat{\Lambda};U,V) = {} & \left(\frac{2\eta}{\mathrm{Re}}(H_\varepsilon(\varphi)(\beta-1)+1)\mathbf{D},\nabla v\right) + (\rho\hat{\mathbf{u}}\cdot\nabla\mathbf{u},v) + \left(\frac{H_\varepsilon(\varphi)}{\mathrm{Re}}\boldsymbol{\tau},\nabla v\right) \\ & -(p,\nabla\cdot v) + (q,\nabla\cdot\mathbf{u}) + 2\mathrm{We}[\mathbf{D}:\mathbf{S}](\mathbf{S},B) + \mathrm{We}(\hat{\mathbf{u}}\cdot\nabla\mathbf{S} - \mathbf{S}\cdot\nabla\hat{\mathbf{u}} - (\nabla\hat{\mathbf{u}})^T\cdot\mathbf{S},B) \\ & + \frac{1}{\boldsymbol{\Lambda}^2}\left[3\alpha\boldsymbol{\Lambda}^4\mathbf{S}\cdot\mathbf{S} + (1-\alpha-3\alpha\boldsymbol{\Lambda}^4\mathrm{tr}(\mathbf{S}\cdot\mathbf{S}))\mathbf{S},B\right] - \frac{1}{\boldsymbol{\Lambda}^2}\left(\frac{1-\alpha}{3}\mathbf{I},B\right) \\ & +(\mathrm{We}\boldsymbol{\Lambda}(\mathbf{D}:\mathbf{S}) - \hat{\mathbf{u}}\cdot\nabla\boldsymbol{\Lambda} - re^{\nu(\boldsymbol{\Lambda}-1)}(\boldsymbol{\Lambda}-1),\chi) \end{aligned}$$

We decompose $U=U_h+U'$, where U_h and U' are, respectively, numerically solved by FEM method and the sub-grid scale method [34].

$$\begin{aligned} & (\mathcal{D}_t(U_h),V_h) + B_h(\mathbf{u}_h,\mathbf{S}_h,\Lambda_h;U_h,V_h) + S_1(\mathbf{u}_h;U_h,V_h) \\ & \qquad + S_2(U_h,V_h) + S_3(\mathbf{u}_h;U_h,V_h) + S_4(u_h;U_h,V_h) = 0 \end{aligned} \tag{18}$$

$$\begin{aligned} S_1(u_h;U_h,V_h) = \sum_K \alpha_1 \Big\langle \tilde{P}[& \rho\hat{\mathbf{u}}_h\cdot\nabla\mathbf{u}_h - \frac{2\eta}{\mathrm{Re}}(H_\varepsilon(\varphi)(\beta-1)+1)\nabla\cdot\mathbf{D}_h - \frac{H_\varepsilon(\varphi)}{\mathrm{Re}}\nabla\cdot\boldsymbol{\tau}_h + \nabla\cdot p_h], \\ & \rho\hat{\mathbf{u}}_h\cdot\nabla v_h - \frac{2\eta}{\mathrm{Re}}(H_\varepsilon(\varphi)(\beta-1)+1)\nabla\cdot\mathbf{D}_{v,h} - \frac{H_\varepsilon(\varphi)}{\mathrm{Re}}(1-\beta)\nabla\cdot v_h + \nabla\cdot q_h \Big\rangle_K \end{aligned}$$

$$S_2(U_h,V_h) = \sum_K \alpha_2 \left\langle \tilde{P}[\nabla\cdot u_h], \nabla\cdot v_h \right\rangle_K$$

$$\begin{aligned} S_3(\tilde{u}_h;U_h,V_h) = \sum_K \alpha_3 \Big\langle \tilde{P}\Big[& \mathrm{We}(\hat{\mathbf{u}}_h\cdot\nabla\mathbf{S}_h - \mathbf{S}_h\cdot\nabla\hat{\mathbf{u}}_h - (\nabla\hat{\mathbf{u}}_h)^T\cdot\mathbf{S}_h) + 2\mathrm{We}[\mathbf{D}_h:\mathbf{S}_h]\mathbf{S}_h \\ & + \boldsymbol{\Lambda}_h^{-2}[3\alpha\boldsymbol{\Lambda}_h^4\mathbf{S}_h\cdot\mathbf{S}_h + (1-\alpha-3\alpha\boldsymbol{\Lambda}_h^4\mathrm{tr}(\mathbf{S}_h\cdot\mathbf{S}_h))\mathbf{S}_h - (1-\alpha)/3\mathbf{I}]\Big], \\ & \mathrm{We}(\hat{\mathbf{u}}_h\cdot\nabla B_h + \nabla\hat{\mathbf{u}}_h\cdot B_h + B_h\cdot(\nabla\hat{\mathbf{u}}_h)^T) + 2\mathrm{We}[\mathbf{D}_h:S_h]B_h \\ & + \boldsymbol{\Lambda}_h^{-2}[3\alpha\boldsymbol{\Lambda}_h^4 S_h\cdot S_h + (1-\alpha-3\alpha\boldsymbol{\Lambda}_h^4\mathrm{tr}(S_h\cdot S_h))B_h - (1-\alpha)/3\mathbf{I}]\Big\rangle_K \end{aligned}$$

$$S_4(u_h;U_h,V_h)=\sum_K \alpha_4 \Big\langle \tilde{P}[\mathrm{We}\boldsymbol{\Lambda}_h(\mathbf{D}_h:\mathbf{S}_h)-\hat{\mathbf{u}}_h\cdot\nabla\boldsymbol{\Lambda}_h-re^{\nu(\boldsymbol{\Lambda}_h-1)}(\boldsymbol{\Lambda}_h-1)],$$
$$\mathrm{We}\chi_h(\mathbf{D}_h:\mathbf{S}_h)-\hat{\mathbf{u}}_h\cdot\nabla\chi_h-re^{\nu(\boldsymbol{\Lambda}_h-1)}(\chi_h-1)\Big\rangle_K$$

$$\alpha_1=\left[c_1\frac{\eta}{h_1^2}+c_2\frac{\rho|u_h|}{h_2}\right]^{-1},\quad \alpha_2=\frac{h_1^2}{c_1\alpha_1},\quad \alpha_3=\left[\frac{c_3}{2\eta}+c_4\left(\frac{\lambda}{2\eta}\frac{|u_h|}{h_2}+\frac{\lambda}{\eta}|\nabla u_h|\right)\right]^{-1},\quad \alpha_4=\left[\frac{c_5}{2\eta}\right]^{-1}.$$

Where α_i, i=1, 2, 3, 4 are adjusting parameters, and the algorithmic parameters c_j, j=1, 2, 3, 4 must be adjusted in the stabilized formulation. The parameters h_1 and h_2 are the characteristic element lengths, the latter is in the streamline direction.

The finite element simulation based on the weak variational formulation given in Eq. (17) can reveal the macro properties of the polymer filling process. In the simulation process, we adopt the Crank-Nicolson-based Split (CNBS) algorithm to study numerically the problem, see Ref. [15] for detailed description.

3.2. Verlet algorithm

Eq. (8) is discretized as [35]:

$$\mathbf{r}_i(t+\Delta t)=\mathbf{r}_i(t)+\Delta t\mathbf{v}_i(t)+\frac{\Delta t^2\mathbf{a}_i(t)}{2} \tag{19}$$

$$\mathbf{v}_i(t+\Delta t/2)=\mathbf{v}_i(t)+\frac{\Delta t\,\mathbf{a}_i(t)}{2} \tag{20}$$

$$\mathbf{v}_i(t+\Delta t)=\mathbf{v}_i(t+\Delta t/2)+\frac{\Delta t\,\mathbf{a}_i(t+\Delta t)}{2} \tag{21}$$

where $\mathbf{V}_i$ and $\mathbf{a}_i$ are, respectively, the speed and acceleration of the particle i.

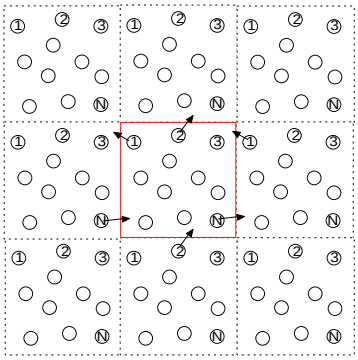

Fig. 2 The sketch of periodic boundary conditions

For the MD simulation, the finite and infinite systems are extremely not similar. However, the simulated system is usually much smaller than the real physical system. Generally, the simulation takes place in a cube cell with periodic boundary to eliminate the

interfacial effects. A periodic system is illustrated in Fig. 2, and the simulation chart is given in Fig. 3.

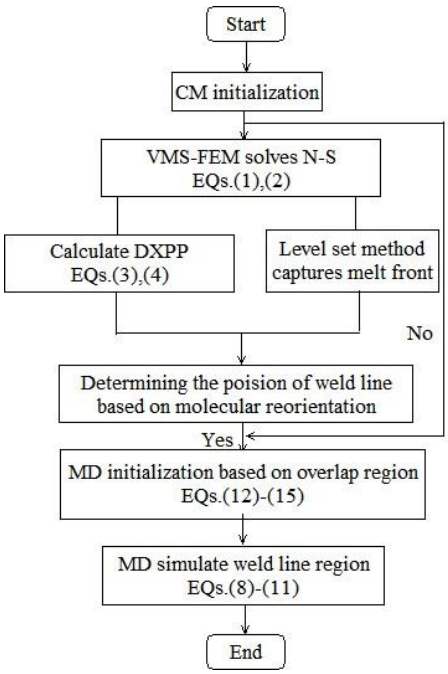

Fig. 3 The flow chart of the coupled numerical method

4. Numerical Results

4.1. Determination of weld lines

For a mold filling process with multiple gates or inserts, the weld lines will be introduced where two or more streams of melts meet with a certain angle to each other in injection molding. In this paper, a 10×1 cavity is used and the two injection gates are symmetrically located on the left and right sides. We use the improved level set method [21] to capture the front interface of polymer melt. Fig. 4 shows the positions of the double gates, the flow direction and the front interface. Moreover, it can be seen that the position of the interface fusion region is about x=5.

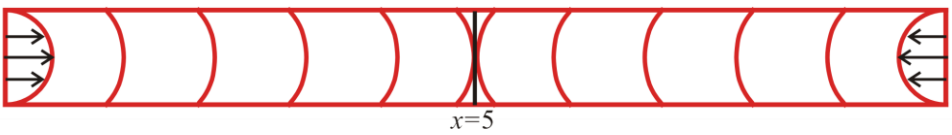

Fig. 4 The positions of the double gates and front interface at different time

For the determination of weld lines, we can obtain the molecular backbone orientation by the DXPP model. Moreover, the molecular backbone orientation of the weld region is vertical orientation to the flow direction. Therefore, we can determinate the position of weld line from the characteristics of the molecular backbone orientation. The ellipse method is used to find the backbone orientation [22]. The molecular backbone orientation in the inlet (a), the boundary (b) and the interface fusion region (c) is shown in the Fig. 5. It can be seen clearly that the molecular backbone orientation in different regions is significantly different. Moreover, there are clearly horizontal orientation and vertical orientation near x=5. Generally, these results indicate that molecular backbones' direction follows the streamline in the center part, whereas molecular backbones' direction is almost perpendicular to the streamline at the weldline. So, we can determinate the position of weld line from the characteristics of the molecular backbone orientation.

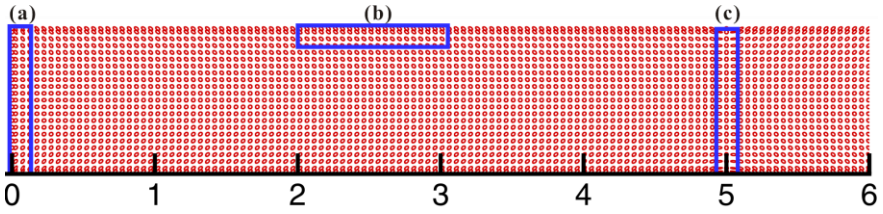

Fig. 5 The molecular backbone orientation of different regions

The weld lines positions are obtained based on the molecular backbone orientation and the level set method [36], respectively. They are shown in Fig. 6 and the weld line positions (blue lines in Fig. 6) are consistent. Therefore, the molecular backbone orientation method is effective for capturing the weld line in the filling process.

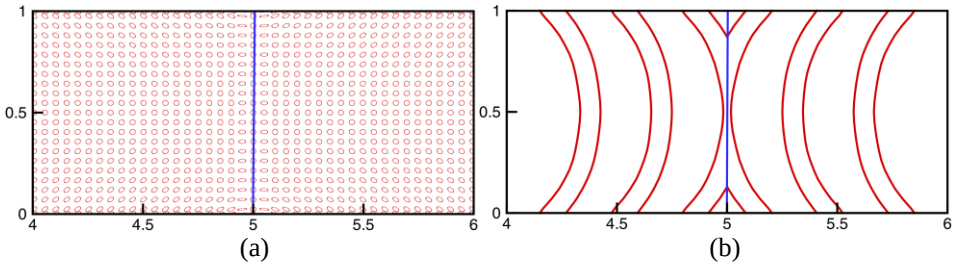

Fig. 6 The position of the weld lines. (a) the molecular backbone orientation;(b) level set method

4.2. The results analysis in weld region

In this sub-section, all variables are the dimensionless forms. The initial chain spatial configurations are zigzag configurations and the number of chains in a cube cell has three cases: one chain, two chains and four chains, as shown in Fig. 7. We assume all chains to have the same length including 8 carbon atoms.

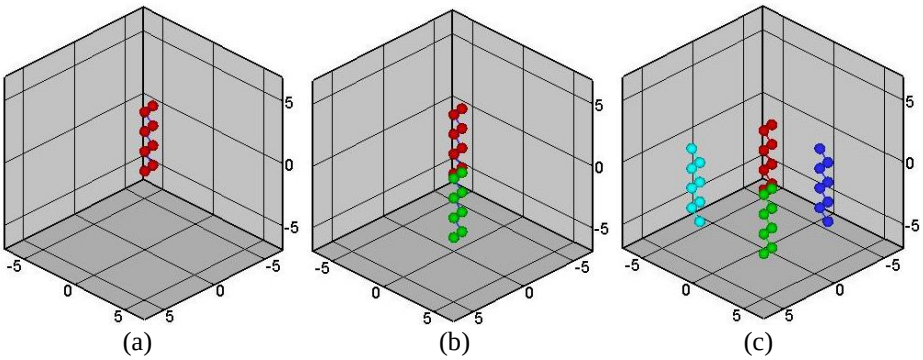

Fig. 7 The initial spatial configurations. (a) one chain; (b) two chains; (c) four chains

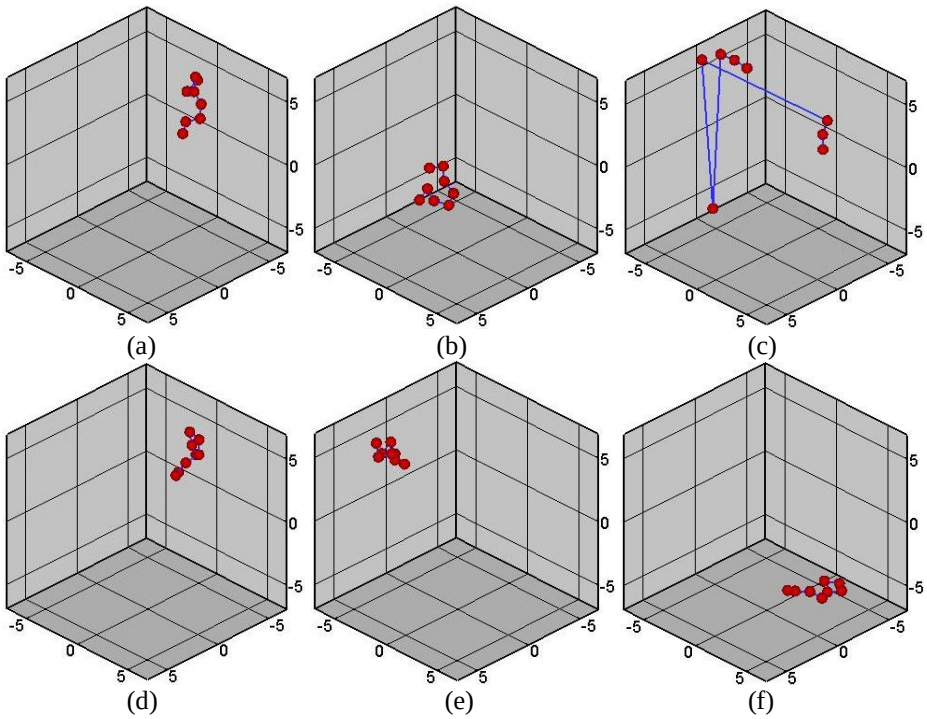

Fig. 8 The spatial configurations of one chain at different times. (a) t=50; (b) t=550; (c) t=1050; (d) t=1550; (e) t=2050; (f) t=2500

The properties of the polymer chain in the weld line region are studied for conformational purposes. The conformational changes and movement process of one chain, two chains and four chains are shown in Fig. 8, Fig. 9 and Fig. 10, respectively, which elucidate that the polymer chain undertakes stretching, orientating, and entangling. Moreover, we can see clearly that the entangling polymer chains will separate again, as shown in Fig. 10.

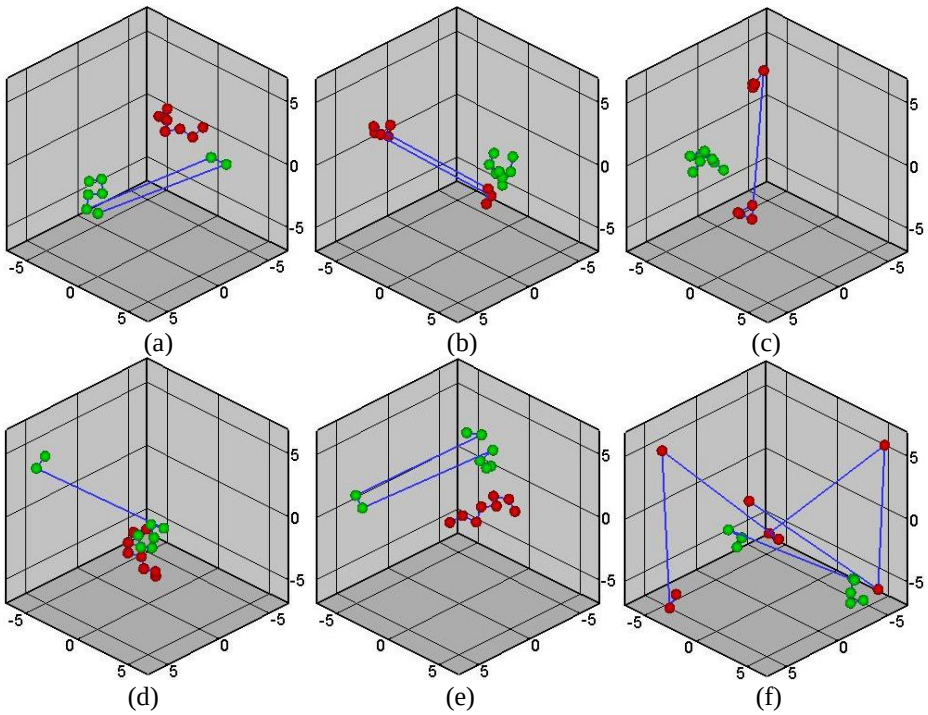

Fig. 9 The spatial configurations of two chains at different times. (a) t=50; (b) t=550; (c) t=1050; (d) t=1550;(e) t=2050; (f) t=2500

To study the molecular chain, the spatial properties of chain conformation are usually investigated by$\langle R^2\rangle$ $\langle S^2\rangle$, and G_{xy}, defined by

$$\begin{cases} \left\langle R^2 \right\rangle = \left\langle | r_n - r_1 |^2 \right\rangle \\ \left\langle S^2 \right\rangle = g_1 + g_2 + g_3 \\ G_{xy} = \dfrac{1}{n}\sum_{i=1}^{n}(r_{ix} - \bar{r}_x)(r_{iy} - \bar{r}_y) \end{cases} \tag{22}$$

where, $\bar{r}$ is the center of mass; g_1, g_2, g_3 are the three eigenvalues of G_{xy}; the ratios of eigenvalues $g_{21}=g_2/g_1$ and $g_{31}=g_3/g_1$ are important factors, when they are different from unity, the distribution is non-spherical.

Fig. 11 shows that the effect of the number of chains and the melt temperature on the bond length (l). It can be seen clearly that a larger number of molecular chains sees a longer bond length, and a higher melt temperature results in a longer bond length as well.

The effects of the number of chains and the melt temperature on $\langle R^2\rangle$ and $\langle S^2\rangle$are shown as in Fig. 12 and Fig. 13, respectively. We can see clearly that they decrease with the increasing of the number of molecular chains and no significant changes about the melt temperature is observed.

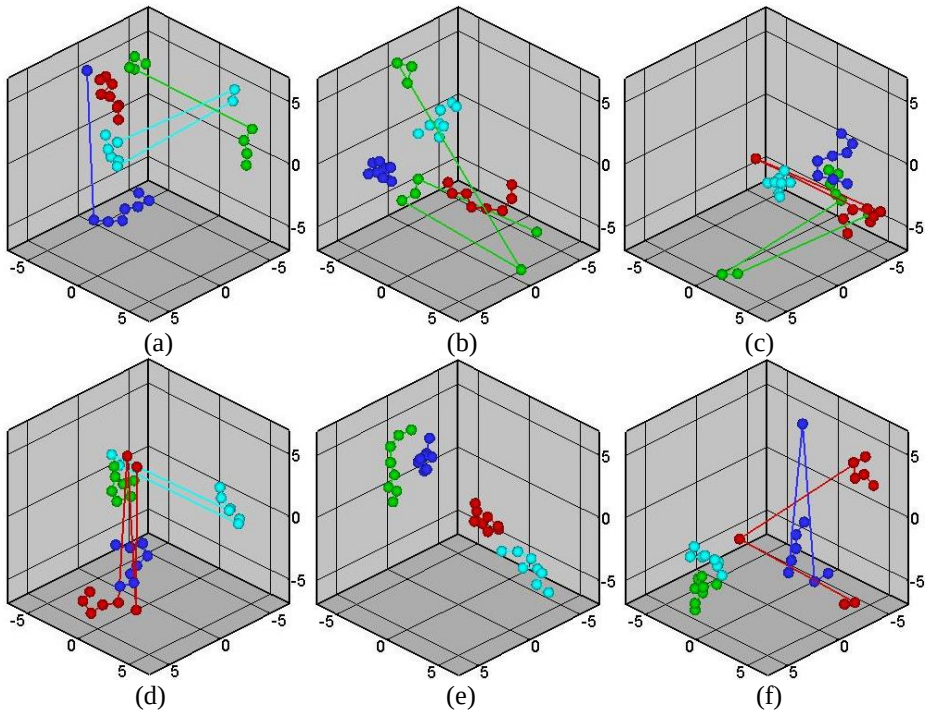

Fig. 10 The spatial configurations of four chains at different times. (a) t=50; (b) t=550; (c) t=1050; (d) t=1550;(e) t=2050;(f) t=2500

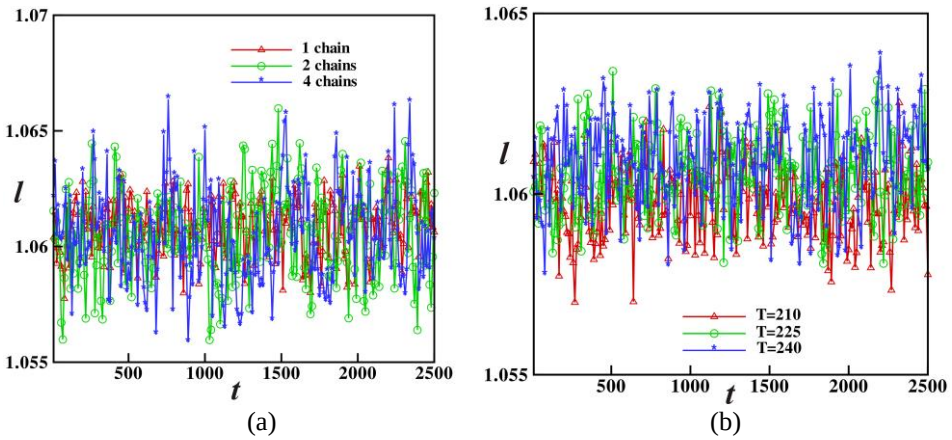

Fig. 11 Influences of the chains' number (a) and the melt temperature (b) on the bond length

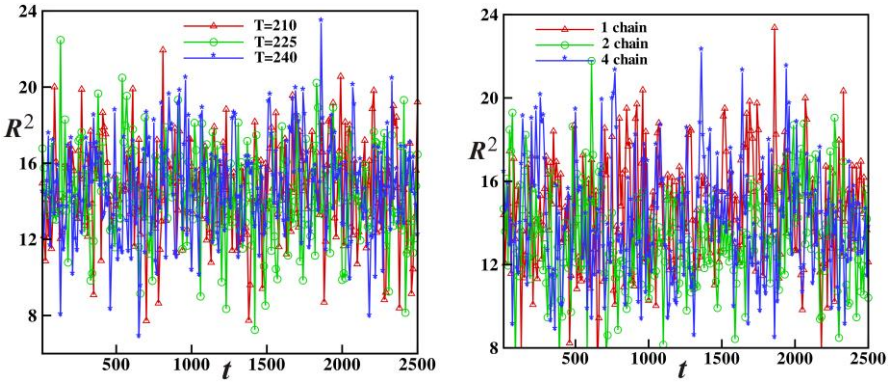

(a) (b)

Fig. 12 Influences of the chains' number (a) and the melt temperature (b) on $\langle R^2 \rangle$

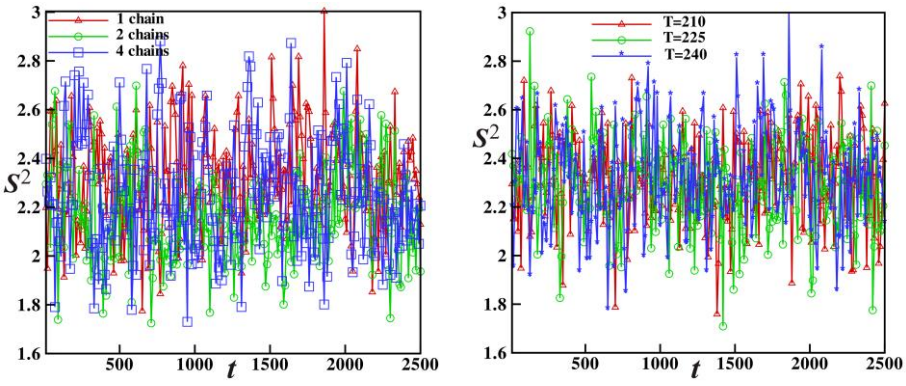

(a) (b)

Fig. 13 Influences of the chains' number (a) and the melt temperature (b) on $\langle S^2 \rangle$

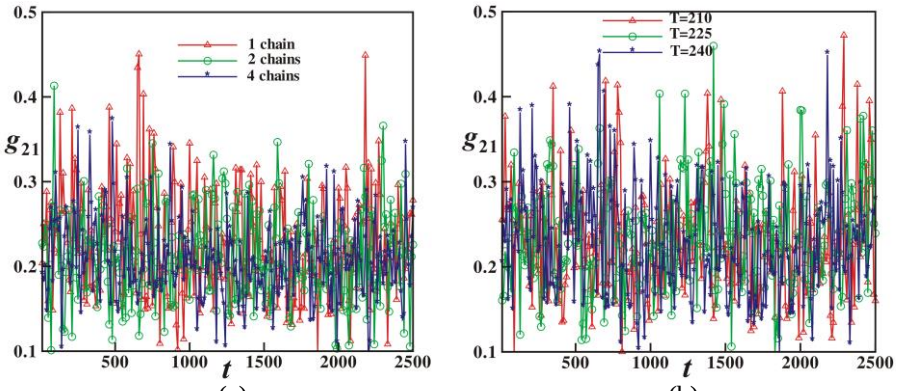

(a) (b)

Fig. 14 Influences of the chains' number (a) and the melt temperature (b) on g_{21}

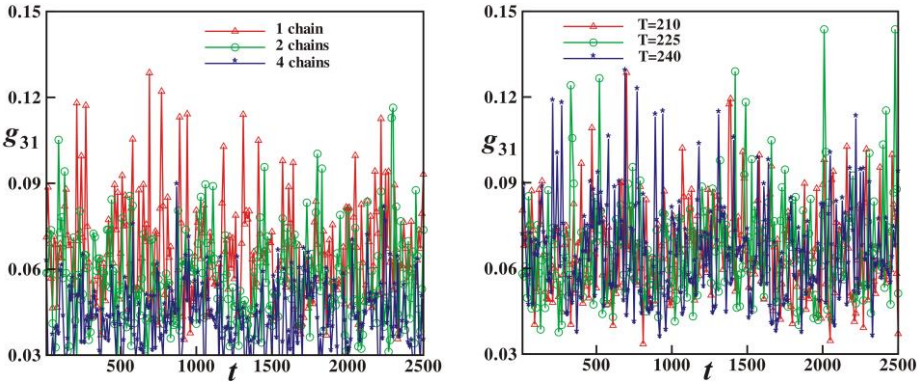

(a) (b)

Fig. 15 Influences of the chains' number (a) and the melt temperature (b) on g_{31}

For the ratios of eigenvalues, Fig. 14 and Fig. 15 show that the values of g_{21} and $g_{31}$are far less than 1, which indicates the mass distribution of polymer chain is non-spherical. Moreover, the ratios decrease with the increasing of the number of molecular chains while no obvious changes with the melt temperature's change.

5. Discussion and Conclusion

A multi-scale coupling model is suggested for simulating the weld line region on a micro scale of the polymer filling process and the other part in a macro scale. The macro scale simulation follows the laws in continuum mechanics, while the micro scale simulation uses the molecular dynamics to reveal the physical understanding of the chains' motion including stretching and entangling. Recently the two-scale concept was further developed into a new mathematical branch called the two-scale fractal calculus [37-39], which studies a same problem, e.g., the polymer filling process, using two differential scales, one is macro scale for continuum mechanics and the other is generally the micro scale of the molecule's size. Seeing with a single scale is always unbelieving [40]. Now the two-scale fractal theory and two-scale thermodynamics have been widely used to study various discontinuous problems [41-45]. Li, et al. established successfully a fractal two-phase flow model for the polymer filling process [46]. Zhou, et al. studied the motion of a drop of ren ink in a saline water [47], though the motion can be easily simulated by the molecular dynamics, the two-scale fractal calculus provides us with an effective tool to the analysis of red ink's motion. The macro scale reveals the main flow property of the studied problem – the red ink will move along the streamlines of the moving fluid, which can be predicted by the laws in continuum mechanics. However, the continuum assumption in fluid mechanics cannot reveal the diffusion of the red ink in water, so another smaller scale of the molecule's size is needed, and the fluid has to be considered as a porous medium, where conversation laws can be established in a fractal space.

In this paper we adopt a weak variational principle, there might not be a genuine variational principle for Navier-Stokes equations, however, we can establish an approximate variational principle for the polymer filling process by the semi-inverse method [48-51], we will discuss it

in a forthcoming paper. Other numerical methods, for examples, the variational iteration method (VIM) [52] and the reducing rank method [53], can also be used for the numerical simulation.

In this paper, we propose two coupling models: the coupling model of the CM and DXPP model and the coupling model of the CM and MD. Moreover, VMS-FEM and Verlet algorithm are used on macro-scale and micro-scale based on the domain decomposition technique, respectively. The molecular backbone orientation can be obtained in the whole filling process by the DXPP model. Therefore, we can determinate the position of the weld line by the molecular backbone orientation's characteristics. Finally, the properties of the polymer chain in the weld line region are studied conformationally and dynamically. The conformational changes and movement process illustrate that the polymer chain undertakes stretching, orientating, and entangling. Moreover, the effect of the number of chains and melt temperature on the spatial properties of chain conformation are investigated. All results show that melt temperature have little impact on molecular chain conformation while the number of molecular chains can affect the spatial properties. Addition, the mass distribution of polymer chain is non-spherical in the weld line region. The multi-scale method can be extended to a two-scale fractal model [36-38].

Acknowledgments: *The paper is a part of the research done within the project of the Young Scientists Fund of the National Natural Science Foundation of China (Grant No.11702206), Natural Science Foundation of Shaan Xi Province(Grant No.2021JQ-492) and Taif University Project (TURSP-2020/16), Saudi Arabia are greatly acknowledged.*

REFERENCES

1. Fellahi, S., Meddad, A., Fisa, B., Favis, B., 1995, *Weldlines in injection-molded parts: A review*, Advances in Polymer Technology: Journal of the Polymer Processing Institute, 14(3), pp. 169-195.
2. Geyer, A., Bonten, C., 2019, *Enhancing the weld line strength of injection molded components*, AIP Conference Proceedings, AIP Publishing LLC, 2055(1), 070023.
3. Minh, P.S., Do, T.T., 2017, *A study on the welding line strength of composite parts with various venting systems in injection molding process*, Key Engineering Materials, 737, pp. 70-76.
4. Li, J., Yang, S.L., Turng, S., Xie, Z., Jiang, S., 2016, *Comparative study of weldline strength in conventional injection molding and rapid heat cycle molding*, Materiale Plastice, 53(3), pp. 448-453.
5. Wang, G., Zhao, G., Wang, X., 2013, *Effects of cavity surface temperature on mechanical properties of specimens with and without a weld line in rapid heat cycle molding*, Materials & Design, 46, pp. 457-472.
6. Mosey, S., Korkees, F., Rees, A., Llewelyn, G., 2019, *Investigation into fibre orientation and weldline reduction of injection moulded short glass-fibre/polyamide 6-6 automotive components*, Journal of Thermoplastic Composite Materials, 33(12), pp. 1603-1628.
7. Hashimoto, S., Kitayama, S., Takano, M., Kubo, Y., Aiba, S., 2020, *Simultaneous optimization of variable injection velocity profile and process parameters in plastic injection molding for minimizing weldline and cycle time*, Journal of Advanced Mechanical Design, Systems, and Manufacturing, 14(3), JAMDSM0029.
8. Baradi, M.B., Cruz, C., Riedel, T., Régnier, G., 2019, *Mechanical and microstructural characterization of flowing weld lines in injection-molded short fiber-reinforced PBT*, Polymer Testing, 74, pp. 152-162.
9. Liao, T., Zhao, X., Yang, X., Whiteside, B.,Coates, P., Jiang, Z., Men, Y., 2019, *Predicting the location of weld line in microinjection-molded polyethylene via molecular orientation distribution*, Journal of Polymer Science Part B: Polymer Physics, 57(24), pp. 1705-1715.
10. Oh, G.H., Jeong, J.H., Park, S.H., Kim, H.S., 2018, *Terahertz time-domain spectroscopy of weld line defects formed during an injection moulding process*, Composites Science and Technology, 157, pp. 67-77.
11. Kalus, J., Jørgensen, J.K., 2014, *Measuring deformation and mechanical properties of weld lines in short fibre reinforced thermoplastics using digital image correlation*, Polymer testing, 36, pp. 44-53.

12. Wang, W., Li, X., Han, X., 2012, *Numerical simulation and experimental verification of the filling stage in injection molding*, Polymer Engineering & Science, 52(1), pp. 42-51.
13. Nguyen Thi, T.B., Yokoyama, A., Ota, K., Kodama, K., Yamashita, K., Isogai, Y., Furuichi, K., Nonomura, C., 2014, *Numerical approach of the injection molding process of fiber-reinforced composite with considering fiber orientation*, AIP Conference Proceedings, American Institute of Physics, 1593(1), pp. 571-577.
14. Yang, B., Ouyang, J., Jiang, T., Liu, C., 2010, *Modeling and simulation of fiber reinforced polymer mold filling process by Level Set method*, CMES - Computer Modeling in Engineering and Sciences, 63(3), pp. 191-222.
15. Li, X., Ouyang, J., Li, Q., Ren, J., 2012, *Simulations of full 3D packing process and flow-induced stresses in injection molding*, Journal of Applied Polymer Science, 126(5), pp. 1532-1545.
16. Cao, W., Min, Z., Zhang, S., Li, H., Wang, Y., Shen, C., 2016, *Numerical simulation for flow-induced stress in injection/compression molding*, Polymer Engineering & Science, 56(3), pp. 287-298.
17. Deng, L., Liang, J., Zhang, Y., Zhou, H., Huang, Z., 2017, *Efficient numerical simulation of injection mold filling with the lattice Boltzmann method*, Engineering Computations, 34(2), pp. 307-329.
18. Farahani, S., Yelne, A., Niaki, F.A., Pilla, S., 2019, *Numerical simulation for the hybrid process of sheet metal forming and injection molding using smoothed particle hydrodynamics method*, SAE Technical Paper, 2019-01-0713.
19. Zhang, Y., Huang, Z., Zhou, H., Li, D., 2015, *A rapid BEM-based method for cooling simulation of injection molding*, Engineering Analysis with Boundary Elements, 52, pp. 110-119.
20. Pashmforoush F., 2020, *Finite Element Analysis of Low Velocity Impact on Carbon Fibers/Carbon Nanotubes Reinforced Polymer Composites*, Journal of applied and computational Mechanics, 6(3), pp. 383-393.
21. Li, X., He, J.H., 2020, *Variational multi-scale finite element method for the two-phase flow of polymer melt filling process*, International Journal of Numerical Methods for Heat & Fluid Flow, 30(3), pp. 1407-1426.
22. Li, X., Zhu, L., Yue, H., 2018, *Multiscale Numerical Simulations of Branched Polymer Melt Viscoelastic Flow Based on Double-Equation XPP Model*, Advances in Mathematical Physics, 2018, 5838290.
23. Rapaport, D.C., Rapaport, D.C.R., 2004, *The art of molecular dynamics simulation*, Cambridge university press, Cambridge, 225 p.
24. Cocker, T., Peller, D., Yu, P., Yu, P., Repp, J., Hube, R., 2016, *Tracking the ultrafast motion of a single molecule by femtosecond orbital imaging*, Nature, 539, pp. 263-267.
25. Zhang, L., Bailey, J.B., Subramanian, R.H., Groisman, A., Tezcan, F.A, 2018, *Hyperexpandable, self-healing macromolecular crystals with integrated polymer networks*, Nature, 557, pp. 86-91.
26. Rabhi, F., Cheng, G., Barriere, T., Aït Hocine, N., 2020, *Influence of elastic-viscoplastic behaviour on the filling efficiency of amorphous thermoplastic polymer during the micro hot embossing process*, Journal of Manufacturing Processes, 59, pp. 487-499.
27. Yasuda, M., Araki, K., Taga, A., Horiba, A., Kawata, H., Hirai, Y., 2011, *Computational study on polymer filling process in nanoimprint lithography*, Microelectronic Engineering, 88(8), pp. 2188-2191.
28. Valiullin, R., Naumov, S., Galvosas, P., Kärger, J., Woo, H.J., Porcheron, F., Monson, P.A., 2006, *Exploration of molecular dynamics during transient sorption of fluids in mesoporous materials*, Nature, 443, pp. 965-968.
29. Zhao, G., Perilla, J., Yufenyuy, E., 2013, *Mature HIV-1 capsid structure by cryo-electron microscopy and all-atom molecular dynamics*, Nature, 497, pp. 643-646.
30. Zepeda-Ruiz, L., Stukowski, A., Oppelstrup, T., Bulatov, V.V., 2017, *Probing the limits of metal plasticity with molecular dynamics simulations*, Nature, 550, pp. 492-495.
31. Sussman, M., Fatemi, E., Smereka, P., Osher, S., 1998, *An improved level set method of incompressible two-phase flows*, Computers & Fluids, 27(5-6), pp. 663-680.
32. Kaminski, G.A., Friesner, R.A., Tirado-Rives, J., 2001, *Evaluation and reparametrization of the OPLS-AA force field for proteins via comparison with accurate quantum chemical calculations on peptides*, The Journal of Physical Chemistry B, 105(28), pp. 6474-6487.
33. Nie, X.B., Chen, S.Y., E., W.N., Robbins, M.O., 2004, *A continuum and molecular dynamics hybrid method for micro- and nano-fluid flow*, Journal of Fluid Mechanics, 500, pp. 55-64.
34. Castillo, E., Codina, R., 2014, *Stabilized stress–velocity–pressure finite element formulations of the Navier–Stokes problem for fluids with non-linear viscosity*, Computer methods in applied mechanics and engineering, 279, pp. 554-578.
35. Groot, R.D., Warren, P.B., 1997, *Dissipative particle dynamics: Bridging the gap between atomistic and mesoscopic simulation*, The Journal of chemical physics, 107(11), pp. 4423-4435.
36. Zheng, S., Ouyang, J., Zhao, Z., 2012, *An adaptive method to capture weldlines during the injection mold filling*, Computers & Mathematics with Applications, 64(9), pp. 2860-2870.

37. He, J.H., Ain, Q.T., 2020, *New promises and future challenges of fractal calculus: from two-scale thermodynamics to fractal variational principle*, Thermal Science, 24(2A), pp. 659-681.
38. Ain, Q.T., He, J.H., 2019, *On two-scale dimension and its applications*, Thermal Science, 23(3), pp. 1707-1712.
39. He, J.H., 2018, *Fractal calculus and its geometrical explanation*, Results in Physics, 10, pp. 272-276.
40. He, J.-H., 2021, *Seeing with a Single Scale is Always Unbelieving: From magic to two-scale fractal*, Thermal Science, 25(2B), pp. 1217-1219.
41. Zuo, Y.T., Liu. H.J. ,2020, *A Fractal Rheological Model for SiC Paste using a Fractal Derivative*, Journal of Applied and Computational Mechanics, 6(SI), pp. 1434-1439.
42. Zuo, Y.T, 2021, *Effect of SiC particles on viscosity of 3D print paste: A Fractal rheological model and experimental verification*, Thermal Science, 25(3B), pp. 2405-2409.
43. Liu, F.J., Zhang, X.J., Li, X., 2019, *Silkworm (Bombyx mori) cocoon vs. wild cocoon multi-layer structure and performance characterization*, Thermal Science, 23(4), pp. 2135-2142.
44. Wang, Y., Yao, S.W., Yang, H.W., 2019, *A fractal derivative model for snow's thermal insulation property*, Thermal Science, 23(4), pp. 2351-2354.
45. He, J.-H., Kou, S.-J., He, C.-H., Zhang, Z.-W., Khaled, A.G., 2021, *Fractal oscillation and its frequency-amplitude property*, Fractals, 29(4), 2150105.
46. Li, X.J., Liu, Z., He, J.H., 2020, *A fractal two-phase flow model for the fiber motion in a polymer filling process*, Fractals, 28(5), 2050093.
47. Zhou, C.J., Tian, D., He, J.H., 2019, *Highly selective penetration of red ink in a saline water*, Thermal Science, 23(4), pp. 2265-2270.
48. He, J.H., 2020, *Variational principle and periodic solution of the Kundu–Mukherjee–Naskar equation*, Results in Physics, 17, 103031.
49. He, J.H., 2021, *On the fractal variational principle for the Telegraph equation*, Fractals, 29(1), 2150022.
50. He, J.H., 2020, *Variational Principle for the Generalized KdV-Burgers Equation with Fractal Derivatives for Shallow Water Waves*, Journal Applied Computational Mechanics, 6(4), pp. 735-740.
51. He, J.-H., Hou, W.-F., Qie, N., Gepreel, K.A., Sedighi, A.H., Mohammad-Sedighi, H., 2021, *Hamiltonian-based frequency-amplitude formulation for nonlinear oscillators*, Facta Universitatis-Series Mechanical Engineering, 19(2), pp. 199-208.
52. He, J.H., Latifizadeh, H., 2020, *A general numerical algorithm for nonlinear differential equations by the variational iteration method*, International Journal of Numerical Methods for Heat and Fluid Flow, 30(11), pp. 4797-4810.
53. He, J.H., El–Dib, Y.O., 2021, *The reducing rank method to solve third-order Duffing equation with the homotopy perturbation*, Numerical Methods for Partial Differential Equations, 37(2), pp. 1800-1808.